NANO LETTERS

pubs.acs.org/NanoLett Letter

Granular Magnetization Switching in Pt/Co/Ti Structure with HfOx Insertion for In-Memory Computing Applications

Tianli Jin,[§] Bo Zhang,[§] Funan Tan, Gerard Joseph Lim, Ze Chen, Jiangwei Cao,* and Wen Siang Lew*

Cite This: *Nano Lett.* 2024, 24, 5521−5528 Read Online

ACCESS | Metrics & More | Article Recommendations | Supporting Information

ABSTRACT: Exploring multiple states based on the domain wall (DW) position has garnered increased attention for in-memory computing applications, particularly focusing on the utilization of spin−orbit torque (SOT) to drive DW motion. However, devices relying on the DW position require efficient DW pinning. Here, we achieve granular magnetization switching by incorporating an HfOx insertion layer between the Co/Ti interface. This corresponds to a transition in the switching model from the DW motion to DW nucleation. Compared to the conventional Pt/Co/Ti structure, incorporation of the HfOx layer results in an enhanced SOT efficiency and a lower switching current density. We also realized stable multistate storage and synaptic plasticity by applying pulse current in the Pt/Co/HfOx/Ti device. The simulation of artificial neural networks (ANN) based on the device can perform digital recognition tasks with an accuracy rate of 91%. These results identify that DW nucleation with a Pt/Co/HfOx/Ti based device has potential applications in multistate storage and ANN.

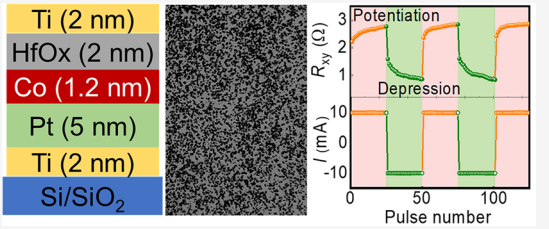

KEYWORDS: *Multiple magnetization states, domain wall nucleation, spin−orbit torque, artificial synapses*

With the emergence of big data, artificial intelligence, and machine learning, there is a high demand for in-memory computing devices with high performance and energy efficiency. Conventional computers use the von Neumann architecture where the main memories are physically and functionally separated from the central processing unit (CPU).[1−3] The mismatch in processing speed and data transfer rate between the CPU and memory constrains the operational efficiency of conventional computers. Inspired by the human brain of storing and processing information concurrently, researchers exploit novel hardware architectures based on emerging nonvolatile memories to implement logic-in-memory architecture.[1,4−8] Compared with other memories, magnetoresistive random-access memory (MRAM) has become one of the most popular candidates for in-memory computing because of its low power consumption, infinite endurance, and nonvolatility.[9−11] The conventional MRAM device based on magnetic tunneling junction (MTJ) has binary states, which is not efficient for operating the multistate storage.[11,12] To achieve the multiple states, researchers have attempted to integrate multi-MTJ pillars into a single write-line.[13,14] Controlling the pillar individually switches to get multiple states, but this requires more MTJ pillars, which greatly increases the bit cell size.[15] Another approach is to control the DW motion in the free layer of MTJ, causing the parallel and antiparallel composition change between the free layer and fixed layer to tune the output resistance.[5,16−18] Recently, the MTJ devices utilizing DW positions for in-memory computing, artificial synapse, and spiking neuron functionalities have been successfully demonstrated.[19−21] However, this method requires larger device sizes and complex device structures to produce multiple DW locations. The presence of multiple DW locations is associated with an increased number of output resistance states for synapses and the realization of neuron functionalities such as leaky integrate-and-fire and self-reset.[22−25] Aside from device fabrication and miniaturization, this approach also poses challenges in the readout window due to the limited tunnel magnetoresistance (TMR) ratio.[11]

The magnetization reversal based on domain nucleation provides gradual switching behavior and paves an alternative solution to achieve the multiple resistance states.[9,26] In the early stages, Fukami et al. introduced the concept of multidomain behavior in the PtMn/$(Co/Ni)_2$ system, which relates to the exchange bias for high DW propagation energy caused by a magnetic field annealing process at 300 °C.[27] Recently, Zhou et al. demonstrated the DW nucleation switching in the $L1_1$-CuPt/CoPt bilayer, which requires high-temperature epitaxial deposition on $SrTiO_3$ (111) substrate.[28] Zhao et al. reported multidomain memristive switching by utilizing He^+ ion irradiation, which is applied through a mask to locally reduce the effective perpendicular anisotropy at a

Received: February 6, 2024
Revised: April 23, 2024
Accepted: April 23, 2024
Published: April 25, 2024

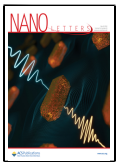

https://doi.org/10.1021/acs.nanolett.4c00662
Nano Lett. 2024, 24, 5521−5528

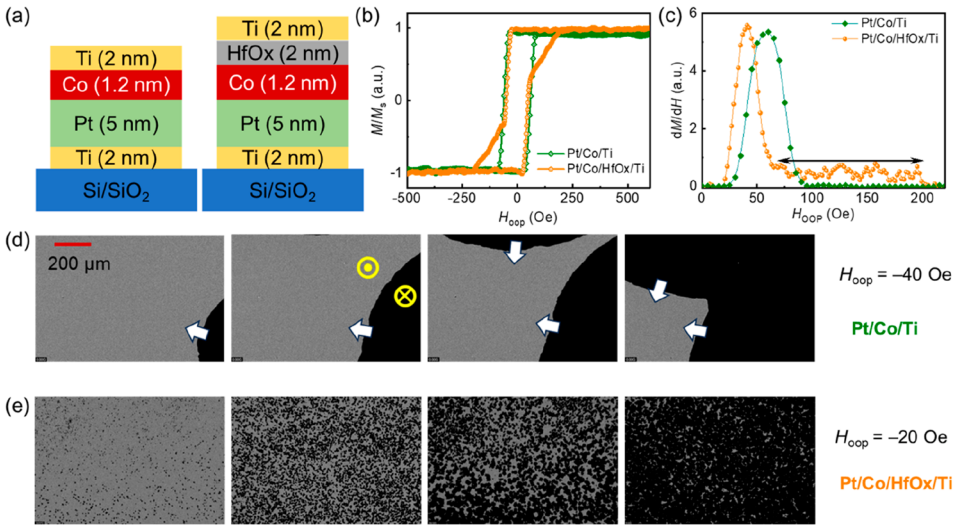

Figure 1. Magnetic properties and magnetization switching images of the Pt/Co/Ti structure with and without the HfOx insertion layer. (a) Schematic of the Pt/Co/Ti and Pt/Co/HfOx/Ti film stacks. (b) Measured hysteresis loops with magnetic field sweeping along the out-of-plane (H_{oop}) direction. (c) Distribution of the magnetization switching field. (d) and (e) Kerr microscopy images of magnetization switching induced by domain wall motion in the Pt/Co/Ti sample and domain nucleation in the Pt/Co/HfOx/Ti sample.

Hall cross W/CoFeB/MgO device.[29] Furthermore, Wan et al. employed Ga^+ ion irradiation to locally modify the anisotropy energy in the Pt/Co/MgO stack, achieving the gradual nucleation switching.[30] Inspired by those observations, we propose incorporating a high oxygen ion mobility oxide layer as the insertion layer at the Co−Ti interface to mitigate interfacial anisotropy energy within the Pt/Co/Ti stack. With the addition of the HfOx insertion layer, the switching mechanism is transitioned from DW motion to DW nucleation. This approach can effectively reduce the complexity of device preparation, offering reliability without being limited to larger devices. The utilization of multiple domain nucleations for achieving multiple states holds promise for designing miniaturized devices. Moreover, the insertion of HfOx can effectively reduce the critical switching current density. With the pulse current inducing granular magnetization switching in the Pt/Co/HfOx/Ti device, we have successfully presented the stable multistate storage and demonstrated the effective functions of synapse plasticity, including long-term potentiation (LTP) and long-term depression (LTD). Furthermore, a three-layer neural network is used to perform the Modified National Institute of Standards and Technology (MNIST) data set handwritten digit recognition task, and the simulated network could achieve a recognition accuracy of about 91%.

Figure 1a presents the Pt/Co/HfOx/Ti stack and the control sample of Pt/Co/Ti. The magnetic hysteresis loops of Pt/Co/HfOx/Ti and Pt/Co/Ti films along the out-of-plane (H_{oop}) direction are characterized by using the vibrating sample magnetometer (VSM), as shown in Figure 1b. The normalized remanence ratio for the two films is up to 95% along the H_{oop} direction, indicating that both samples have a perpendicular magnetization anisotropy (PMA). In contrast to the sharp switching observed in the Pt/Co/Ti structure, the switching behavior in the Pt/Co/HfOx/Ti structure exhibits a long tail. Additionally, a wide distribution of the switching field within the range of 75 to 200 Oe is observed in the Pt/Co/HfOx/Ti sample, as presented in Figure 1c. Next, polar Kerr imaging of the switching process is conducted while applying the H_{oop}, as shown in Figure 1d and e, where the gray and dark regions represent the domain pointing in the up and down directions, respectively. In the Pt/Co/Ti sample, a pulsed field of −40 Oe is applied, resulting in the nucleation of a dark domain at one boundary, which subsequently grows larger with the continuous application of the same pulsed field. The DW motion leads to the sharp switching as observed in the $M-H_{oop}$ loop in the Pt/Co/Ti sample.[31−33] However, granular magnetization switching is observed in the Pt/Co/HfOx/Ti sample, as revealed by Kerr imaging. The number of nucleated dark domains rapidly increases with the continuous application of the pulsed field instead of undergoing magnetization reversal via DW motion. This granular magnetization switching in the Pt/Co/HfOx/Ti sample provides multiple magnetization states, which is consistent with the observed long tail switching behavior and the wide distribution of the switching field, as shown in Figure 1b and 1c. The mechanism of the granular switching is ascribed to the partial oxidation of the Co layer, resulting in an inhomogeneous nucleation energy. This, in turn, leads to a switching process characterized by multiple domain nucleation.[34] Unlike the Pt/Co/Ti film, it expands upon the appearance of a single reversal domain without initiating additional domain nucleation. Introducing a HfOx insertion layer between the Co/Ti interface also results in a reduction in the anisotropy energy (K_u). Additionally, with the Ti capped layer on HfOx, which possesses a higher affinity for oxygen than Co, Ti absorbs oxygen from the HfOx layer.[35] This induces the spatial variation of oxygen content along the Co/HfOx interface, consequently modifying the K_u. Those combined effects of inhomogeneous nucleation energy and reduced anisotropy contribute to the observed granular behavior. The size of the nucleated domain for Pt/Co/HfOx/Ti sample has been estimated to be around 1.4 μm from the Kerr images. However, this estimated value is much larger than its actual size due to the limited pixel resolution of the MOKE CCD camera. Further details about the calculation of anisotropy energy, the crystallinity of the Co layer, estimation of domain size, and sheet resistance of the films after inserting

https://doi.org/10.1021/acs.nanolett.4c00662
Nano Lett. 2024, 24, 5521−5528

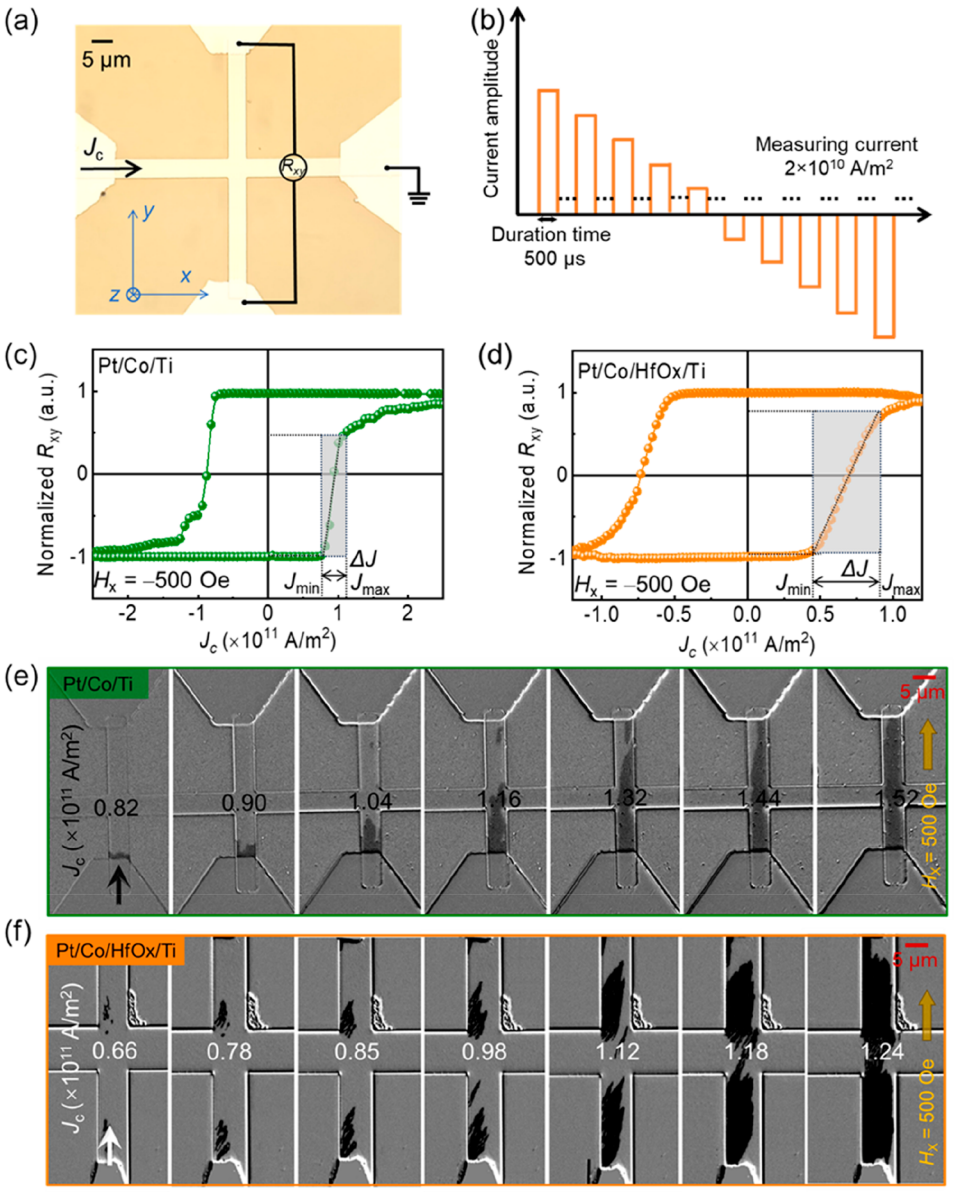

Figure 2. Current induced magnetization switching. (a) Optical image of the Hall bar device. (b) Schematic measurement procedure of the pulse-current-induced magnetization reversal. Measured Hall resistance changes with applied pulse current density for (c) Pt/Co/Ti and (d) Pt/Co/HfOx/Ti samples under an external magnetic field of $H_x = -500$ Oe. Insets show the region of the ΔJ. (e) MOKE images reveal DW motion driven by current in the Pt/Co/Ti sample. (f) MOKE images reveal domain nucleation driven by current in the Pt/Co/HfOx/Ti sample.

the HfOx layer have been discussed in Supporting Information S1 to S4.

After the characterization of magnetic properties, the film stacks are subsequently patterned into Hall bar devices by using electron-beam lithography and ion milling techniques, as shown in Figure 2a. Current-induced magnetization switching is carried out in the Hall bar devices, where a constant in-plane magnetic field (H_x) is applied along the current channel of the Hall bar (x direction). A series of current pulses (J_c) with a pulse width of 500 μs is injected into the device, as depicted in Figure 2b. Between the two adjacent pulses, a test current density of 2×10^{10} A/m^2 is used to measure the Hall resistance (R_{xy}), which enables the monitoring of the magnetization states.[18,36] The thermal effect on pulse currents generated in the Pt/Co/HfOx/Ti device has been discussed in Supporting Information S5. Figure 2c and d display the current-induced magnetization reversal curves for the two samples under $H_x = -500$ Oe. Simultaneously, the magnetization switching evolution process is captured by Kerr microscopy with an increasing pulse current density, as illustrated in Figure 2e and f. As depicted in the MOKE images of Figure 2e, a dark reversal domain appears at the bottom edge in the Pt/Co/Ti Hall bar device when the pulse current density reaches 0.82×10^{11} A/m^2. Consequently, the dark domain expands with increasing current density, leading to a complete reversal process. The switching curve exhibits a "slight tail" with the further increase of the current strength to 1.22×10^{11} A/m^2, which is consistent with the switching mechanism involving DW motion, and the observed "slight tail" is due to the edge pinning effect.[37,38] For the Pt/Co/HfOx/Ti sample, the resistance change of the magnetization reversal curve is continuous, which is expected of continuous nucleation

https://doi.org/10.1021/acs.nanolett.4c00662
Nano Lett. 2024, 24, 5521−5528

mode.[28,30] Upon application of a pulse current, the reversal domain is nucleated from the edge region, as shown in Figure 2f. With an increase in the amplitude of the pulse current, there is a corresponding increase in the number of nucleated dark domains, accompanying the expansion of existing domains. The Pt/Co/HfOx/Ti stack exhibits a gradual switching behavior, accompanied by an increase in the number of resistance states. Moreover, the linear variation region of the magnetization reversal curve for the two samples, $\Delta J = J_{max} - J_{min}$, is quantitatively calculated, which is the difference between the minimum current required to change the R_{xy} (J_{min}) value, and the maximum current within the linear change of the R_{xy} (J_{max}) value,[39,40] as shown in the insets of Figure 2c and d. The Pt/Co/HfOx/Ti sample has a wider linear variation region, up to 5.81×10^{10} A/m^2, compared to that of the Pt/Co/Ti sample, with $\Delta J = 2.91 \times 10^{10}$ A/m^2, indicating more multiresistance states. The critical switching current density of the two samples has been summarized, and the details are presented in Supporting Information S6. After inserting the HfOx layer with high oxygen ion mobility,[41] there is an effective reduction in the critical switching current density from 9.27×10^{10} A/m^2 to 6.12×10^{10} A/m^2. Inserting the HfOx layer can indeed lead to changes in magnetic properties of Co such as saturation magnetization (M_s), K_u, switching current density, and pinning field, also resulting in a reduction of DW velocity in the Pt/Co/HfOx/Ti sample.[21] The main reason for the broadening of ΔJ is the larger distribution of the magnetization switching field.

Harmonic Hall voltage measurements are conducted to investigate the reduction in J_{sw} for the structure with the HfOx insertion layer. In this measurement, an AC current with a frequency of 307 Hz is applied along the x direction. The in-plane field is applied along the longitudinal (x) or transverse (y) direction. These are employed to analyze the damping-like field (H_{DL}) or field-like field (H_{FL}) effective fields by neglecting the contribution of the planar Hall effect.[42,43] Both the first (V_ω) and second ($V_{2\omega}$) harmonic Hall voltages are collected simultaneously. H_{DL} and H_{FL} can be calculated through $H_{DL} = -2\left(\frac{dV_{2\omega}}{dH_x}\right)/\left(\frac{d^2V_\omega}{dH_x^2}\right)$ and $H_{FL} = -2\left(\frac{dV_{2\omega}}{dH_y}\right)/\left(\frac{d^2V_\omega}{dH_y^2}\right)$. Figure 3a presents typical Hall voltage from harmonic measurements,

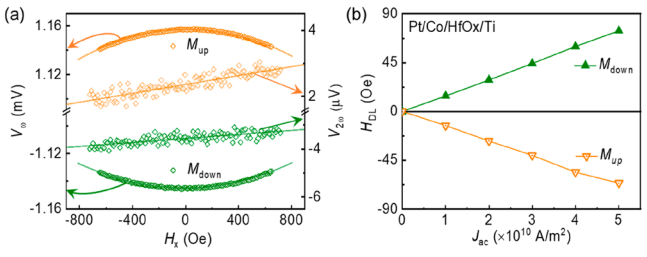

Figure 3. Characterization of spin−orbit torque (SOT) efficiency of the Pt/Co/HfOx/Ti sample. (a) Measured first and second harmonic voltages with sweeping in-plane magnetic field H_x. (b) Calculated current density (J_{ac}) dependence of the damping-like field (H_{DL}).

including the V_ω and $V_{2\omega}$ as a function of H_x, obtained from the Pt/Co/HfOx/Ti device with $J_{ac} = 2 \times 10^{10}$ A/m^2. Figure 3b shows H_{DL} as a function of increasing AC current density J_{ac}, where M_{down} and M_{up} indicate the initial magnetization directions. In both cases, H_{DL} with J_{ac} exhibits good linearity.[31] To comprise the SOT efficiency, the damping-like field efficiency χ of two stacks is extracted, where χ is defined as H_{DL}/J_{ac}. The χ_{DL} increases from 9.1 to 11.5 Oe/(10^{10}A/m^2) with the addition of the HfOx insertion layer. The higher SOT efficiency achieved in the Pt/Co/HfOx/Ti sample is due to the enhanced interfacial spin−orbit coupling between the Co and HfOx layers, and the oxygen-induced orbital hybridization at the Co/HfOx interface.[44−46] More discussion is presented in Supporting Information S7.

In addition to the high efficiency, the Pt/Co/HfOx/Ti sample exhibits a wider linear region during magnetization reversal and lower critical switching current density. These characteristics indicate better potential for applications in multistate storage and ANN.[18,28,47] Evaluation of the non-volatile multistate property and assessment of device functionality as an artificial synapse is conducted for the Pt/Co/HfOx/Ti sample. First, a series of pulse currents with maximum magnitudes (I_{max}) ranging from 10 to 18 mA (corresponding to the current density ranging from 0.66×10^{11} to 1.18×10^{11} A/m^2) is applied to the Pt/Co/HfOx/Ti sample under the external field of −500 Oe, resulting in a sequence of minor switching curves and multiple magnetization states, as shown in Figure 4a. These results demonstrate that the final magnetization status can be tuned by the pulse current through the SOT magnitudes. Next, continuous manipulation of the magnetization state by varying pulse current magnitudes and polarities is carried out. In this experiment, a series of pulse currents with different amplitudes are applied to the Pt/Co/HfOx/Ti sample, and the R_{xy} values are recorded after each pulse, as shown in Figure 4b and c. With an increasing amplitude of the positive or negative current pulse, the R_{xy} value increases or decreases. The results indicate that the SOT is able to bidirectionally manipulate the multiple magnetization states in the Pt/Co/HfOx/Ti sample. It should be noted that an external magnetic field is required for the SOT-driven memristor behavior in the Pt/Co/HfOx/Ti structure. To advance the integration of the Pt/Co/HfOx/Ti system into network architectures, we propose replacing the SOT generation layer, Pt, with noncollinear antiferromagnets such as Mn_3Sn, which can generate out-of-plane antidamping torque and provide the field-free switching of the Co layer.[48] Another efficient approach is to adjust the asymmetric current density distribution at Pt/Co/HfOx/Ti crossbar array devices to induce a spin current gradient for field-free granular switching.[49,50] Implementing both approaches within the Co/HfOx/Ti system demonstrates promise in achieving field-free granular switching, making them well-suited for efficient network architectures in practical applications.

The artificial neural network is composed of multiple layers of neurons, and the adjacent neurons are connected through artificial synapses, as illustrated in Figure 4d, and the weight is updated by changing the connection strength.[4,6,52] The weight value should be modulated continuously and be nonvolatile. Moreover, the variations of Hall resistance, which are continuously tuned by programming consecutive pulse sequences, are desired to imitate synaptic behavior. As shown in Figure 4e, a series of six pulses lists (25 current pulses per list) with positive and negative polarity for different current amplitudes but the same pulse width of 500 μs is applied along the x-axis to stimulate the artificial synapses. It is observed that as the number of positive current pulses increases, the R_{xy} value increases gradually. When the current polarity is reversed, the R_{xy} value decreases gradually. These results suggest that the synaptic behavior of LTP and LTD can

https://doi.org/10.1021/acs.nanolett.4c00662
Nano Lett. 2024, 24, 5521−5528

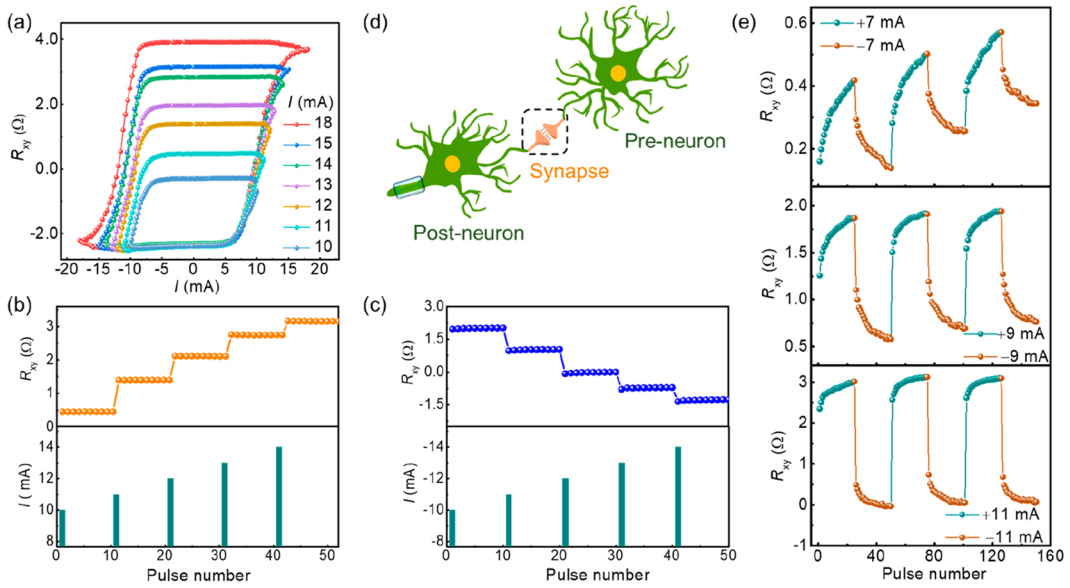

Figure 4. Multiple resistance states induced by current in the Pt/Co/HfOx/Ti device. (a) Hall resistance R_{xy} with pulse current loops with varying maximum current magnitude, from 10 to 18 mA, under $H_x = -500$ Oe. (b and c) Multiple R_{xy} states tuned by a series of positive and negative current pulses, respectively. (d) Schematic diagram of biological synapses and neurons. (e) Demonstration of LTP and LTD corresponding to R_{xy} using varied pulse numbers and pulse currents of ±7 mA, ± 9 mA, and ±11 mA.

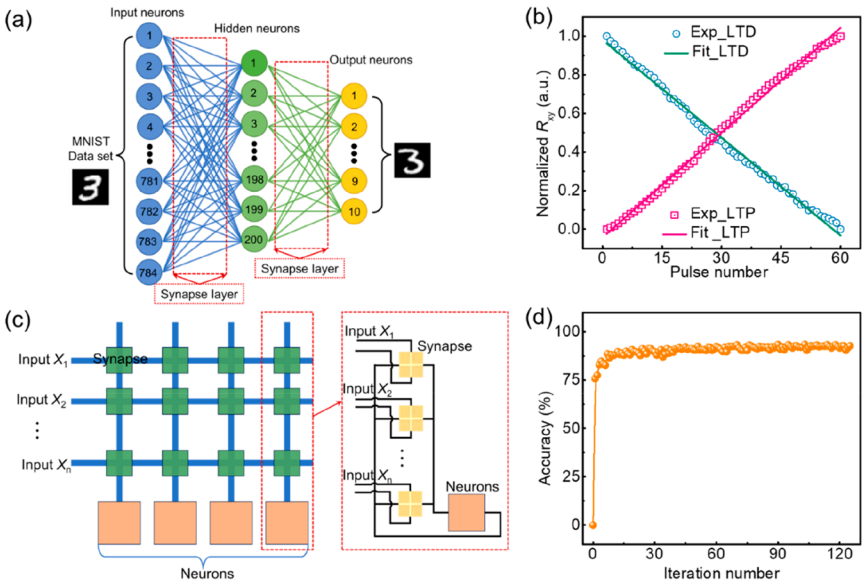

Figure 5. Simulation of artificial neural networks. (a) Schematic diagram of the artificial neural network simulation structure. (b) Demonstration of long-term potentiation (LTP) and long-term depression (LTD) for the synapse. (c) Schematic of the incorporation of Hall bar devices into the crossbar array and the circuit diagram. (d) Evolution of identification accuracy for the digital number based on the resistance value in the Pt/Co/HfOx/Ti synaptic device.

be simulated by modulating the R_{xy} value through current pulses. An asymmetric behavior between the LTP and LTD has been observed, which correlates with the asymmetry in the magnetization reversal curve. This asymmetry arises from differences in the DW propagation velocity under positive and negative current pulses, attributed to the inhomogeneous distribution of pinning sites in the Hall-bar devices.[18] In addition, the phenomenon of our sample with different amplitudes of current pulses can be used to achieve synaptic behavior. A stronger stimulus leads to a larger variation of synaptic weight by comparing the applied current of ±7 mA and ±11 mA, as demonstrated in Figure 4e. Operating at a low current of ±7 mA, partial magnetization switching occurs, resulting in a random domain state. Consequently, the maximum or minimum value of R_{xy} varies accordingly. However, applying a current of ±11 mA triggers full magnetization switching, resulting in the repeatable maximum or minimum value of R_{xy}. For practical applications in ANN, a reset current is required to eliminate the effect of different initial states, thereby ensuring that each write state is the same. Additionally, an additional circuit reprogramming is necessary

https://doi.org/10.1021/acs.nanolett.4c00662
Nano Lett. 2024, 24, 5521−5528

to reset the initial resistance state, further enhancing the reliability and reproducibility of the device operation.

Next, we exploited the Pt/Co/HfOx/Ti device to simulate the ANN for handwritten digit recognition. Figure 5a shows the working principle of the three-layer ANN for realizing the function of handwritten digit recognition. In each recognition process, the handwritten digital picture is converted into 28 × 28 pixels, which is converted into 784 voltage signals as the input of the neural network. The 10 output neurons correspond to the output numbers of 0 to 9. Studies have shown that nonidentical pulses can lead to much more linear LTP and LTD than identical pulses for spintronic devices.[52,53] Therefore, in this work, nonidentical pulses with amplitudes ranging from 9 to 15 mA are used to investigate synaptic plasticity. The R_{xy} gradually increases or decreases with increasing the amplitude of negative or positive pulses, as shown in Figure 5b, which excellently simulates the synaptic activities of the LTP and LTD. The value of R_{xy} linearly increasing (decreasing) with the pulse number not only performs continuously adjustable behavior but also shows good symmetric behavior in both polarities. The Hall bar devices are integrated into the crossbar array framework to perform the MNIST handwritten digit recognition task, as illustrated in Figure 5c. The circuit diagram for the artificial synapses is also presented in Figure 5c.[54] In this step, the input signal (X_n) is represented by the pulse current, leading to a change of the synaptic weights at the Hall detection electrode. Subsequently, the accumulated changes from all the weights in the same column gather to generate a Hall resistance or Hall voltage. The obtained total Hall voltage is appropriately adjusted to supply a suitable output to the next neuron stage. Using the measured synaptic plasticity of our device, we conduct the MNIST handwritten digit recognition task. Moreover, we also demonstrated the sigmoidal neurons application with the Pt/Co/HfOx/Ti device, which has been included in Supporting Information S8. Figure 5d shows the accuracy of the ANN for the MNIST handwritten digit recognition task as a function of the number of iterations. Our simulations reveal that the ANN can reach a recognition accuracy of about 91.5%. Therefore, the demonstrated device has the potential to function as an artificial synapse and be exploited for ANN construction.

In summary, we report the achievement of SOT-induced nonvolatile multistate storage and simulation of artificial synapses in the Pt/Co/HfOx/Ti sample. Through the introduction of an HfOx insertion layer at the Co/Ti interface, an enhancement of SOT efficiency and a 34% reduction of critical switching current density is achieved. Moreover, the mechanism of magnetization reversal undergoes a transition from DW motion in the Pt/Co/Ti sample to granular magnetization switching in the Pt/Co/HfOx/Ti sample. The multistate storage and function of synapse plasticity are successfully demonstrated by utilizing the granular magnetization switching observed in the Pt/Co/HfOx/Ti stack. The simulated ANN based on such synapses achieves a high recognition accuracy of about 91%. Our work paves the way for high-efficiency SOT-driven memory devices and their applications in in-memory computing.

■ ASSOCIATED CONTENT

Supporting Information

The Supporting Information is available free of charge at https://pubs.acs.org/doi/10.1021/acs.nanolett.4c00662.

Additional discussion on the anisotropy energy K_u calculation from hysteresis loops, X-ray diffraction analysis of Pt/Co/Ti stack with HfOx insertion layer, estimation of nucleated domain size in Pt/Co/HfOx/Ti device, sheet resistance of Pt/Co/Ti stack with HfOx insertion layer, thermal effect on current-induced magnetization switching, comparison of critical switching current of Pt/Co/Ti and Pt/Co/HfOx/Ti devices, characterization of SOT efficiency of Pt/Co/Ti and Pt/Co/HfOx/Ti samples, demonstration of Pt/Co/HfOx/Ti device for sigmoidal neurons application, methods of sample growth and preparation, measurements of Kerr images, current-induced magnetization switching, SOT efficiency and simulation of handwritten digit recognition. (PDF)

■ AUTHOR INFORMATION

Corresponding Authors

Jiangwei Cao − *Key Laboratory for Magnetism and Magnetic Materials of the Ministry of Education, Lanzhou University, Lanzhou 730000, China*; Email: caojw@lzu.edu.cn

Wen Siang Lew − *School of Physical and Mathematical Sciences, Nanyang Technological University, Singapore 637371, Singapore*; orcid.org/0000-0002-5161-741X; Email: wensiang@ntu.edu.sg

Authors

Tianli Jin − *School of Physical and Mathematical Sciences, Nanyang Technological University, Singapore 637371, Singapore*; orcid.org/0000-0002-9364-6024

Bo Zhang − *School of Physical and Mathematical Sciences, Nanyang Technological University, Singapore 637371, Singapore; Key Laboratory for Magnetism and Magnetic Materials of the Ministry of Education, Lanzhou University, Lanzhou 730000, China*

Funan Tan − *School of Physical and Mathematical Sciences, Nanyang Technological University, Singapore 637371, Singapore*

Gerard Joseph Lim − *School of Physical and Mathematical Sciences, Nanyang Technological University, Singapore 637371, Singapore*; orcid.org/0000-0003-2411-5841

Ze Chen − *School of Physical and Mathematical Sciences, Nanyang Technological University, Singapore 637371, Singapore*

Complete contact information is available at: https://pubs.acs.org/10.1021/acs.nanolett.4c00662

Author Contributions

[§]T.J. and B.Z. contributed equally to this work.

Notes

The authors declare no competing financial interest.

■ ACKNOWLEDGMENTS

This work was supported by the RIE2020 ASTAR AME IAF-ICP grant (No. I1801E0030) and MOE Tier 1 grant (No. RG76/23).

■ REFERENCES

(1) Yao, P.; Wu, H.; Gao, B.; Eryilmaz, S. B.; Huang, X.; Zhang, W.; Zhang, Q.; Deng, N.; Shi, L.; Wong, H.-S. P.; Qian, H.; et al. Face classification using electronic synapses. *Nat. Commun.* **2017**, *8*, 15199.

(2) Maddu, R.; Kumar, D.; Bhatti, S.; Piramanayagam, S. N. Spintronic Heterostructures for Artificial Intelligence: A Materials Perspective. *Phys. Status Solidi - Rapid Res. Lett.* **2023**, *17* (6), 2200493.
(3) Zou, X.; Xu, S.; Chen, X.; Yan, L.; Han, Y. Breaking the von Neumann bottleneck: architecture-level processing-in-memory technology. *Sci. China Inf. Sci.* **2021**, *64* (6), 160404.
(4) Liu, L.; Dananjaya, P. A.; Ang, C. C. I.; Koh, E. K.; Lim, G. J.; Poh, H. Y.; Chee, M. Y.; Lee, C. X. X.; Lew, W. S. A bi-functional three-terminal memristor applicable as an artificial synapse and neuron. *Nanoscale* **2023**, *15* (42), 17076−17084.
(5) Sengupta, A.; Shim, Y.; Roy, K. Proposal for an All-Spin Artificial Neural Network: Emulating Neural and Synaptic Functionalities Through Domain Wall Motion in Ferromagnets. *IEEE Trans Biomed Circuits Syst.* **2016**, *10* (6), 1152−1160.
(6) Shen, J. X.; Shang, D. S.; Chai, Y. S.; Wang, S. G.; Shen, B. G.; Sun, Y. Mimicking Synaptic Plasticity and Neural Network Using Memtranstors. *Adv. Mater.* **2018**, *30* (12), No. e1706717.
(7) Zhang, Y.; Zhang, Z.; Lin, K.; Zheng, Z.; Feng, X.; Zhao, W. Spintronic devices towards advanced computing framework. In *2023 IEEE Nanotechnology Materials and Devices Conference (NMDC)*, 2023; IEEE: pp 208−209.
(8) Yang, Z.; He, K.; Zhang, Z.; Lu, Y.; Li, Z.; Wang, Y.; Wang, Z.; Zhao, W. A novel computing-in-memory platform based on hybrid spintronic/CMOS memory. *IEEE Trans. Electron Devices* **2022**, *69* (4), 1698−1705.
(9) Chen, B.; Zeng, M.; Khoo, K. H.; Das, D.; Fong, X.; Fukami, S.; Li, S.; Zhao, W.; Parkin, S. S.P.; Piramanayagam, S.N.; Lim, S. T. Spintronic devices for high-density memory and neuromorphic computing-A review. *Mater. Today* **2023**, *70*, 193−217.
(10) Zhou, J.; Chen, J. Prospect of spintronics in neuromorphic computing. *Adv. Electron. Mater.* **2021**, *7* (9), 2100465.
(11) Cai, K.; Jin, T.; Lew, W. S. Spin-based magnetic random-access memory for high-performance computing. *Natl. Sci. Rev.* **2024**, *11* (3), nwad272.
(12) Wang, C.; Wang, Z.; Zhang, Z.; Zhang, Y.; Zhao, W. Area and Energy Efficient Short-Circuit-Logic-Based STT-MRAM Crossbar Array for Binary Neural Networks. *IEEE Transactions on Circuits and Systems II: Express Briefs* **2024**, *71* (3), 1386−1390.
(13) Cai, K.; Van Beek, S.; Rao, S.; Fan, K.; Gupta, M.; Nguyen, V. D.; Jayakumar, G.; Talmelli, G.; Couet, S.; Kar, G. S. Selective operations of multi-pillar SOT-MRAM for high density and low power embedded memories. In 2022 IEEE Symposium on VLSI Technology and Circuits (VLSI Technology and Circuits), 2022, IEEE: pp 375−376.
(14) Doevenspeck, J.; Garello, K.; Verhoef, B.; Degraeve, R.; Van Beek, S.; Crotti, D.; Yasin, F.; Couet, S.; Jayakumar, G.; Papistas, I. SOT-MRAM based analog in-memory computing for DNN inference. In *2020 IEEE Symposium on VLSI Technology*, 2020, IEEE: pp 1−2.
(15) Doevenspeck, J.; Garello, K.; Rao, S.; Yasin, F.; Couet, S.; Jayakumar, G.; Mallik, A.; Cosemans, S.; Debacker, P.; Verkest, D.; Lauwereins, R. Multi-pillar SOT-MRAM for accurate analog in-memory DNN inference. In 2021 Symposium on VLSI Technology, 2021, IEEE: pp 1−2.
(16) Yang, M.; Li, Y.; Luo, J.; Deng, Y.; Zhang, N.; Zhang, X.; Li, S.; Cui, Y.; Yu, P.; Yang, T. All-Linear Multistate Magnetic Switching Induced by Electrical Current. *Phys. Rev. Appl.* **2021**, *15* (5), 054013.
(17) Kumar, D.; Chung, H. J.; Chan, J.; Jin, T.; Lim, S. T.; Parkin, S. S. P.; Sbiaa, R.; Piramanayagam, S. N. Ultralow Energy Domain Wall Device for Spin-Based Neuromorphic Computing. *ACS Nano* **2023**, *17* (7), 6261−6274.
(18) Zhang, B.; Lv, W.; Guo, Y.; Wang, B.; Luo, K.; Li, W.; Cao, J. Realization of Multi-Level State and Artificial Synapses Function in Stacked $(Ta/CoFeB/MgO)_N$ Structures. *Adv. Electron. Mater.* **2023**, *9* (2), 2200939.
(19) Siddiqui, S. A.; Dutta, S.; Tang, A.; Liu, L.; Ross, C. A.; Baldo, M. A. Magnetic domain wall based synaptic and activation function generator for neuromorphic accelerators. *Nano Lett.* **2020**, *20* (2), 1033−1040.
(20) Wang, D.; Tang, R.; Lin, H.; Liu, L.; Xu, N.; Sun, Y.; Zhao, X.; Wang, Z.; Wang, D.; Mai, Z.; et al. Spintronic leaky-integrate-fire spiking neurons with self-reset and winner-takes-all for neuromorphic computing. *Nat. Commun.* **2023**, *14* (1), 1068.
(21) Lin, H.; Xu, N.; Wang, D.; Liu, L.; Zhao, X.; Zhou, Y.; Luo, X.; Song, C.; Yu, G.; Xing, G. Implementation of Highly Reliable and Energy-Efficient Nonvolatile In-Memory Computing using Multistate Domain Wall Spin-Orbit Torque Device. *Adv. Intell. Syst.* **2022**, *4* (9), 2200028.
(22) Wang, D.; Wang, Z.; Xu, N.; Liu, L.; Lin, H.; Zhao, X.; Jiang, S.; Lin, W.; Gao, N.; Liu, M.; Xing, G.; et al. Synergy of Spin-Orbit Torque and Built-In Field in Magnetic Tunnel Junctions with Tilted Magnetic Anisotropy: Toward Tunable and Reliable Spintronic Neurons. *Adv. Sci.* **2022**, *9* (30), No. e2203006.
(23) Raymenants, E.; Bultynck, O.; Wan, D.; Devolder, T.; Garello, K.; Souriau, L.; Thiam, A.; Tsvetanova, D.; Canvel, Y.; Nikonov, D. E.; et al. Nanoscale domain wall devices with magnetic tunnel junction read and write. *Nat. Electron.* **2021**, *4* (6), 392−398.
(24) Wang, Z.; Wang, D.; Liu, L.; Jiang, S.; Chai, G.; Cao, J.; Xing, G. Tilted magnetic anisotropy-tailored spin torque nano-oscillators for neuromorphic computing. *Appl. Phys. Lett.* **2023**, *123*, 204101.
(25) Wang, D.; Wang, Z.; Jiang, S.; Liu, L.; Lin, H.; Zhang, Y.; Tang, R.; Luo, X.; Xing, G. Field-free domain wall spin torque nano-oscillators with multimodal real-time modulation and high-quality factor. *Materials Today Electronics* **2023**, *6*, 100065.
(26) Zhang, B.; Wu, Y.; Zeng, X.; Guo, Y.; Wang, B.; Cao, J. The optimized memristor performance by utilizing the constrained domain wall motion in Pt/Co-Tb/Ta structure. *J. Appl. Phys.* **2021**, *129* (22), 223901.
(27) Fukami, S.; Zhang, C.; DuttaGupta, S.; Kurenkov, A.; Ohno, H. Magnetization switching by spin-orbit torque in an antiferromagnet-ferromagnet bilayer system. *Nat. Mater.* **2016**, *15* (5), 535−541.
(28) Zhou, J.; Zhao, T.; Shu, X.; Liu, L.; Lin, W.; Chen, S.; Shi, S.; Yan, X.; Liu, X.; Chen, J. Spin-Orbit Torque-Induced Domain Nucleation for Neuromorphic Computing. *Adv. Mater.* **2021**, *33* (36), No. e2103672.
(29) Zhao, X.; Liu, Y.; Zhu, D.; Sall, M.; Zhang, X.; Ma, H.; Langer, J.; Ocker, B.; Jaiswal, S.; Jakob, G.; et al. Spin-orbit torque driven multi-level switching in He^+ irradiated W/CoFeB/MgO Hall bars with perpendicular anisotropy. *Appl. Phys. Lett.* **2020**, *116* (24), 242401.
(30) Wan, C. H.; Stebliy, M. E.; Wang, X.; Yu, G. Q.; Han, X. F.; Kolesnikov, A. G.; Bazrov, M. A.; Letushev, M. E.; Ognev, A. V.; Samardak, A. S. Gradual magnetization switching via domain nucleation driven by spin-orbit torque. *Appl. Phys. Lett.* **2021**, *118* (3), 032407.
(31) Wu, S.; Jin, T. L.; Tan, F. N.; Ang, C. C. I.; Poh, H. Y.; Lim, G. J.; Lew, W. S. Enhancement of spin-orbit torque in Pt/Co/HfOx heterostructures with voltage-controlled oxygen ion migration. *Appl. Phys. Lett.* **2023**, *122* (12), 122403.
(32) Zhang, R.; Liao, L.; Chen, X.; Xu, T.; Cai, L.; Guo, M.; Bai, H.; Sun, L.; Xue, F.; Su, J. Current-induced magnetization switching in a CoTb amorphous single layer. *Phys. Rev. B* **2020**, *101* (21), 214418.
(33) Ang, C. C. I.; Gan, W.; Wong, G. D. H.; Lew, W. S. Temperature-modulated magnetic skyrmion phases and transformations analysis from first-order reversal curve study. *Phys. Rev. B* **2021**, *103* (14), 144409.
(34) Fassatoui, A.; Ranno, L.; PenaGarcia, J.; Balan, C.; Vogel, J.; Béa, H.; Pizzini, S. Kinetics of Ion Migration in the Electric Field-Driven Manipulation of Magnetic Anisotropy of Pt/Co/Oxide Multilayers. *Small* **2021**, *17* (38), 2102427.
(35) Li, W.; Tuo, Y.; Mi, W.; Wang, D.; Wang, M.; Zhou, L.; Zhao, J. The effect of oxygen affinity electrode Ti on the performance of vanadium oxide-based valence change resistive random access memory. *Vacuum.* **2023**, *209* (2023), 111794.
(36) Jin, T.; Gan, W.; Tan, F.; Sernicola, N. R.; Lew, W. S.; Piramanayagam, S. Synaptic element for neuromorphic computing using a magnetic domain wall device with synthetic pinning sites. *J. Phys. D: Appl. Phys.* **2019**, *52* (44), 445001.

https://doi.org/10.1021/acs.nanolett.4c00662
Nano Lett. 2024, 24, 5521−5528

(37) Li, D.; Cui, B.; Yun, J.; Chen, M.; Guo, X.; Wu, K.; Zhang, X.; Wang, Y.; Mao, J.; Zuo, Y. Current-induced domain wall motion and tilting in perpendicularly magnetized racetracks. *Nanoscale Res. Lett.* **2018**, *13*, 1−7.
(38) Liu, L.; Song, Y.; Zhao, X.; Liu, W.; Zhang, Z. Full-Scale Field-Free Spin-Orbit Torque Switching in HoCo Structure with a Vertical Composition Gradient. *Adv. Funct. Mater.* **2022**, *32* (39), 2200328.
(39) Borders, W. A.; Akima, H.; Fukami, S.; Moriya, S.; Kurihara, S.; Horio, Y.; Sato, S.; Ohno, H. Analogue spin-orbit torque device for artificial-neural-network-based associative memory operation. *Appl. Phys. Express* **2017**, *10* (1), 013007.
(40) Li, W.; Lan, X.; Liu, X.; Zhang, E.; Deng, Y.; Wang, K. Switching plasticity in compensated ferrimagnetic multilayers for neuromorphic computing. *Chin. Phys. B* **2022**, *31* (11), 117106.
(41) Ma, L.; Wu, J.; Zhu, T.; Huang, Y.; Lu, Q.; Liu, S. Ultrahigh oxygen ion mobility in ferroelectric hafnia. *Phys. Rev. Lett.* **2023**, *131*, 256801.
(42) Jin, T.; Lim, G. J.; Poh, H. Y.; Wu, S.; Tan, F.; Lew, W. S. Spin reflection-induced field-free magnetization switching in perpendicularly magnetized MgO/Pt/Co heterostructures. *ACS Appl. Mater. Interfaces* **2022**, *14* (7), 9781−9787.
(43) Poh, H. Y.; Ang, C. C. I.; Gan, W.; Lim, G. J.; Lew, W. S. Direct spin accumulation quantification in ferromagnetic heterostructures using DC bias harmonic Hall measurement. *Phys. Rev. B* **2021**, *104* (22), 224416.
(44) Kageyama, Y.; Tazaki, Y.; An, H.; Harumoto, T.; Gao, T.; Shi, J.; Ando, K. Spin-orbit torque manipulated by fine-tuning of oxygen-induced orbital hybridization. *Sci. Adv.* **2019**, *5* (11), No. eaax4278.
(45) Chen, X.; Liu, Y.; Yang, G.; Shi, H.; Hu, C.; Li, M.; Zeng, H. Giant antidamping orbital torque originating from the orbital Rashba-Edelstein effect in ferromagnetic heterostructures. *Nat. Commun.* **2018**, *9* (1), 2569.
(46) Yang, L.; Fei, Y.; Zhou, K.; Chen, L.; Fu, Q.; Li, L.; Yan, C.; Li, H.; Du, Y.; Liu, R. Maximizing spin-orbit torque efficiency of Ta (O)/Py via modulating oxygen-induced interface orbital hybridization. *Appl. Phys. Lett.* **2021**, *118* (3), 032405.
(47) Yun, J.; Bai, Q.; Yan, Z.; Chang, M.; Mao, J.; Zuo, Y.; Yang, D.; Xi, L.; Xue, D. Tailoring multilevel-stable remanence states in exchange-biased system through spin-orbit torque. *Adv. Funct. Mater.* **2020**, *30* (15), 1909092.
(48) Hu, S.; Shao, D. F.; Yang, H.; Pan, C.; Fu, Z.; Tang, M.; Yang, Y.; Fan, W.; Zhou, S.; Tsymbal, E. Y.; Qiu, X. Efficient perpendicular magnetization switching by a magnetic spin Hall effect in a noncollinear antiferromagnet. *Nat. Commun.* **2022**, *13*, 447.
(49) Deng, Y.; Li, W.; Lan, X.; Zhang, E.; Li, R.; Shang, Y.; Liu, S.; Li, B.; Liu, X.; Zheng, H.; Wang, K.; et al. Field-Free Switching of Spin Crossbar Arrays by Asymmetric Spin Current Gradient. *Adv. Funct. Mater.* **2024**, *34*, 2307612.
(50) Cai, K.; Yang, M.; Ju, H.; Wang, S.; Ji, Y.; Li, B.; Edmonds, K. W.; Sheng, Y.; Zhang, B.; Zhang, N.; et al. Electric field control of deterministic current-induced magnetization switching in a hybrid ferromagnetic/ferroelectric structure. *Nat. Mater.* **2017**, *16*, 712−716.
(51) Markram, H.; Lübke, J.; Frotscher, M.; Sakmann, B. Regulation of synaptic efficacy by coincidence of postsynaptic APs and EPSPs. *Science* **1997**, *275* (5297), 213−215.
(52) Zhang, Q.; Zhao, Y.; He, C.; Huo, Y.; Cui, B.; Zhu, Z.; Zhang, G.; Yu, G.; He, B.; Zhang, Y. Perpendicular Magnetization Switching Driven by Spin-Orbit Torque for Artificial Synapses in Epitaxial Pt-Based Multilayers. *Adv. Electron. Mater.* **2022**, *8* (12), 2200845.
(53) Yadav, R. S.; Gupta, P.; Holla, A.; Ali Khan, K. I.; Muduli, P. K.; Bhowmik, D. Demonstration of synaptic behavior in a heavy-metal-ferromagnetic-metal-oxide-heterostructure-based spintronic device for on-chip learning in crossbar-array-based neural networks. *ACS Appl. Electron. Mater.* **2023**, *5* (1), 484−497.
(54) Yang, S.; Shin, J.; Kim, T.; Moon, K.-W.; Kim, J.; Jang, G.; Hyeon, D. S.; Yang, J.; Hwang, C.; Jeong, Y.; Hong, J. P. Integrated neuromorphic computing networks by artificial spin synapses and spin neurons. *NPG Asia Mater.* **2021**, *13* (1), 11.

https://doi.org/10.1021/acs.nanolett.4c00662
Nano Lett. 2024, 24, 5521−5528